# Thermal infrared image analysis of a quiescent cone on Piton de la Fournaise volcano: Evidence of convective air flow within an unconsolidated soil

R. Antoine, David Baratoux, M. Rabinowicz, F. Fontaine, Patrick Bachèlery, Thomas Staudacher, G Saracco, Anthony Finizola

# Thermal infrared image analysis of a quiescent cone on Piton de la Fournaise volcano: Evidence of convective air flow within an unconsolidated soil

R. Antoine [a,*], D. Baratoux [a], M. Rabinowicz [a], F. Fontaine [b], P. Bachèlery [c], T. Staudacher [d], G. Saracco [e], A. Finizola [c]

[a] Observatoire Midi-Pyrénés, UMR 5562 CNRS, Laboratoire Dynamique Terrestre et Planétaire, Université Toulouse III, Toulouse, France
[b] Institut de Physique du Globe, Equipe Géosciences Marines, Paris, France
[c] Géosciences Réunion, UMR 7154 CNRS, Faculté des Sciences et Technologies, Université de la Réunion, St Denis, Ile de La Réunion, France
[d] Observatoire Volcanologique du Piton de La Fournaise, Insitut de Physique du Globe de Paris, Ile de la Réunion, France
[e] Centre Européeen de Recherche et d'Enseignement des Géosciences de l'Environnement UMR 6635 CNSR, Aix-en-Provence, France

A B S T R A C T

We report on the detection of air convection with infrared thermal images for two quasi-circular craters, 20 m and 40 m wide, forming the volcanically inactive cone of Formica Leo (Reunion Island). The thermal images have been acquired from an infrared camera at regular time intervals during a complete diurnal cycle. During the night and at dawn, we observe that the rims are warmer than the centers of the craters. The conductivity contrast of the highly porous soils filling the craters and their $30^{\circ}$ slopes are unable to explain the systematic temperature drop from rim to centers. We suggest that this signal could be attributed to air convection with gas entering the highly permeable soil at the center of each crater, then flowing upslope along the bottom of the soil layer, before exiting it along the crater rims. To quantify this process, we present a two-dimensional numerical modelling of air convection in a sloped volcanic soil with a surface temperature evolving between day and night This convection depends on a unique dimensionless equivalent Rayleigh number $Ra_{cq}$ which is the product of the standard Rayleigh number with the volumetric heat capacity ratio of the air and the soil. The convective flow is unsteady: during some periods, the convective flow is entirely confined within the soil, and at other times air enters the crater at its center and exits it at the rim crests. When $Ra_{cq}$ =6000, a value likely compatible with the soil permeability and the geothermal heat flux. a very strong transient cold air plume occasionally develops along the center of the crater. The interval of time between two plumes only depends on the thermal fluctuations within the top boundary layer of the convective cell, and thus is not contrasted by the diurnal cycle. The detachment of a cold plume can occur at any time, after few days of quiescence, and lasts several hours. During the whole convective cycle, the rim to center temperature drop persists and has an amplitude and a shape having an excellent agreement with that found in the IR-images. This work constitutes a preliminary step to explore the deep thermal structure of the active caldera of Bory-Dolomieu and could help to improve the understanding of volcanic hazards of the Reunion volcano.

## 1. Introduction

In 2001, a helicopter flyby was done just before sunrise over Enclos Fouqué, the caldera of Piton de la Fournaise (Fig. 1). IR images were acquired during the flyby and striking observations were found at a small volcanically inactive scoria cone, Formica Leo. This 250 years-old ellipsoidal structure (major axis: 115 m, minor axis: 80 m) is composed of 2 unconsolidated and highly eroded subcircular craters (Fig. 2). The South East crater is 40 m in diameter and 15 m deep. The North West crater is smaller and shallower measuring 22 m in diameter and 5 m deep. Fine lapillis ($d \approx 0.5$ cm) cover the rims of each crater (Fig. 3a). Their inner and outer flanks are covered by coarse lapillis ($d \approx 5$ cm) and the slopes are near the 30° angle of repose. The bottoms of both craters are filled with aggregates — highly porous assemblage of the fine lapillis — which are $d \approx 10$ cm size blocks (Fig. 3b). Some parts of the external flanks are deeply incised by erosion. Finally, some zones on the internal flanks are filled with highly permeable scorias locally covered by fine lapillis (Fig. 2b). The whole Formica Leo structure is embayed within a flat and highly fissurated platform of massive basalts (Fig. 2a and b) sparsely covered with lapillis.

IR data have usually been used to discriminate geological facies (Myers et al., 1969; Sabins, 1969; Rowan et al., 1970; Watson, 1973, 1975). However, a first examination of Formica Leo IR images revealed

* Corresponding author. Tel.: +33 0561333024.
E-mail address: antoine@dtp.obs-mip.fr (R. Antoine).

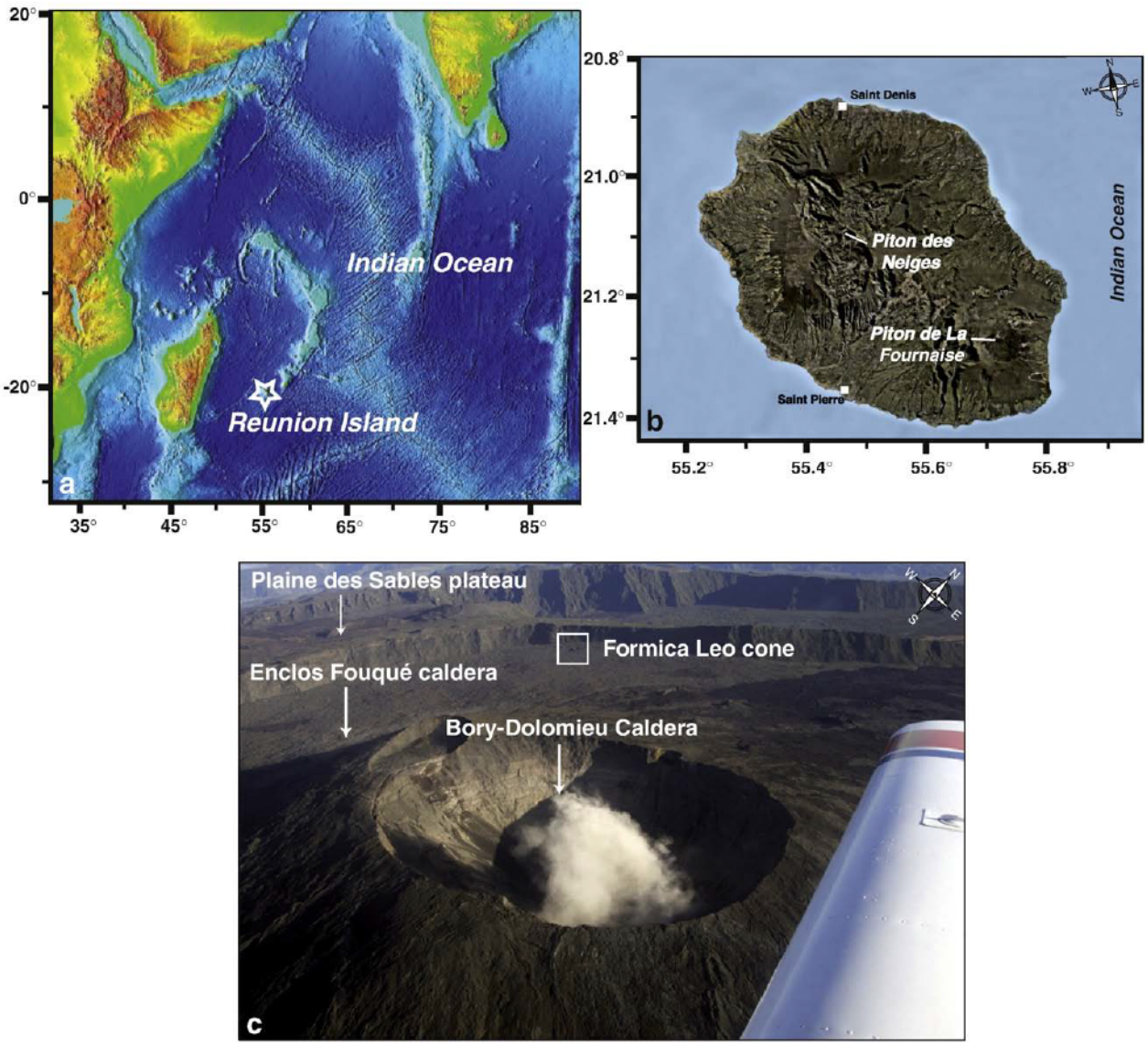


**Fig. 1.** a) Location of Reunion Island and b) Piton des Neiges and Piton de La Fournaise volcanoes; c) Aerial view of Piton de La Fournaise volcano and location of Plaine des Sables plateau, Enclos Fouqué caldera, Bory–Dolomieu summit and Formica Leo cone study site (photo taken by Frédéric Caillé).

temperature patterns in apparent contradiction with the variations of thermal surface properties. At this preliminary stage, a possible link with subsurface thermal processes was suggested. Between eruptions, the heat of the volcano is partly lost by conduction and advection through fumerolles, hot springs or phreatomagmatic events. The high temperatures associated to these areas are easily detected and mapped from a single thermal image. The evolution of the activity can be recorded by weekly, monthly or yearly observations. Outside of these areas, heat is also discharged to a lesser extent and is more difficult to detect. Indeed, the temperature perturbations remain in the range of the diurnal surface temperature variations. The detection of this heat flow is thus not possible from a single thermal image, and only few experiments have been done with such objectives (Bonneville et al., 1985; Brivio et al., 1989).

To overcome this problem, we obtained repeated field observations during one diurnal cycle and conducted thermal modelling of the surface and subsurface heat transport. In Section 2, we present IR images of Formica Leo acquired over several days as well as the procedure to separate the contribution of the diurnal cycle based on the evolution of these temperature fields. We estimate the thermal diffuvisity and porosity of Formica Leo soil from thermal data acquired with ground probes in Plaine Des Sables inactive area, a flat surface of Piton de la Fournaise volcano, with a similar soil granulometry to Formica Leo (Section 1). Then, we evaluate the influence of the cone topography on the surface temperatures (Section 4). These studies show that the observed rim to crater center temperature contrast is opposite to that induced by the topography and at least 5 °C to 10 °C too large to be attributed to surface properties.

Since the soil at Formica Leo is clearly saturated with air, the subsurface heat transport can only be attributed to convective porous air flow. In Section 5, we present a numerical model of this convection within an inclined rectangular box approximating the geometry of the porous media below the surface of the crater. The numerical model takes into account the physical properties of the soil, the topography and the diurnal evolution of temperature. The model easily explains the observed temperature contrast between the rim crest and the craters centers at Formica Leo. To scale the model, we compare measured subsurface temperatures across the South East crater with predicted ones. Finally, a comparison between computed and observed Darcy velocities of the flow using anemometry is presented.

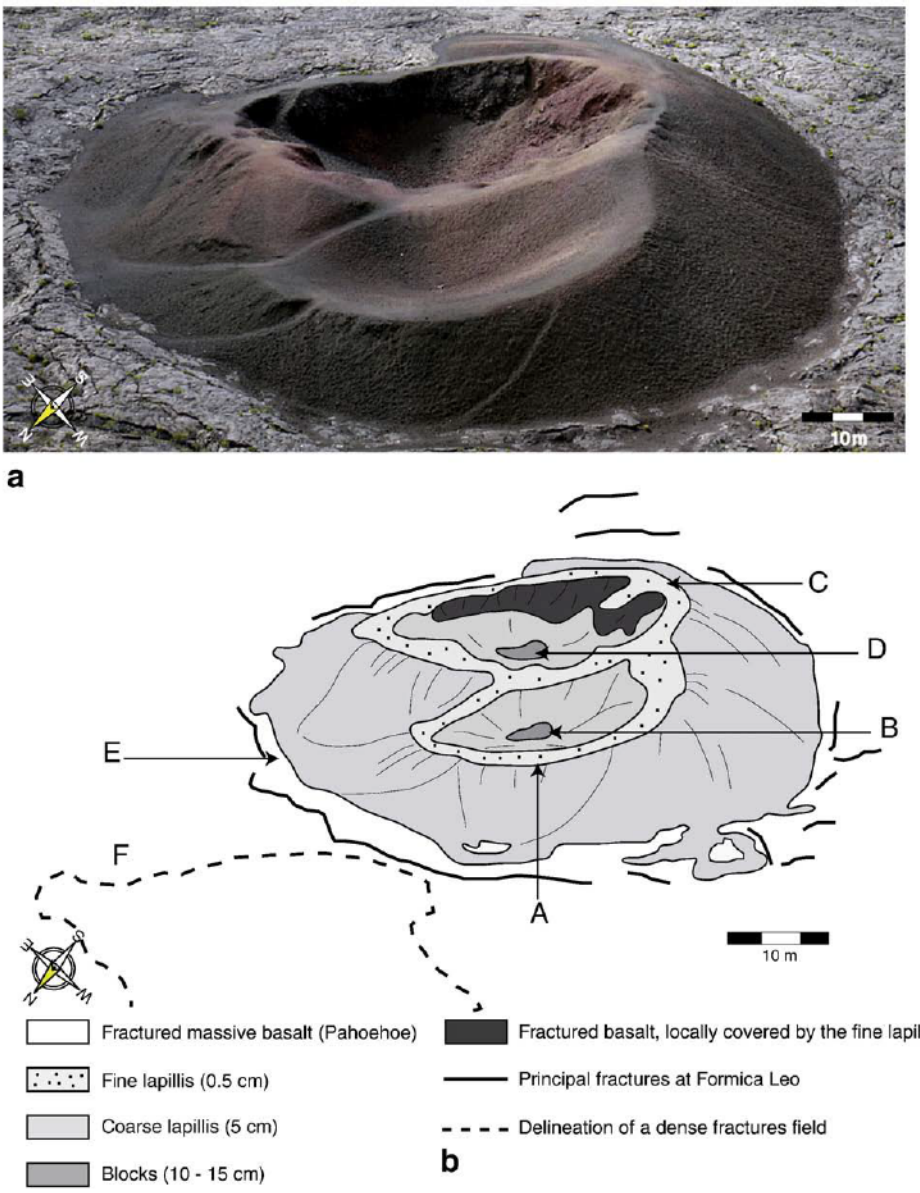


**Fig. 2.** a) Formica Leo cone and its surroundings. The picture is taken from the rim crest of Enclos Fouqué. b) Map of the different classes of material of Formica Leo: A,B sites are located on the rim crest and on the bottom of the NW crater, respectively; C,D sites are located on the rim crest and on the bottom of the SE crater, respectively; E, F zones are outside Formica Leo on the flat plateau of Enclos Fouqué. This plateau is composed of fine lapillis from Formica Leo in E, and massive basalt in F.

This cross check between observations and modelling allows us to definitively demonstrate that the heat steadily provided by the volcano is actively transported by a porous air convective flow within Formica Leo. In the last section of the paper, we consider possible consequences of these processes on the general heat transport in the whole structure, particularly the Bory Dolomieu caldera.

## 2. Infrared data and their processing

The infrared survey was conducted in 2006, from April, 24th, 6 p.m. to April, 25th, noon. A camera was placed along Enclos Fouqué rim (Fig. 2) at a height of 100 m above Formica Leo approximately 150 m away, optimizing both the resolution and the angle of view amongst the possible observation points. The sky was partly cloudy and the wind was weak. We used a digital FLIR ThermaCam PM 695 camera owned by the *Observatoire Volcanologique du Piton de la Fournaise*. The instrument uses an uncooled microbolometer technology to measure radiations in the range of 7.5 to 13 μm. The surface temperatures measured by the camera are corrected from the effects of the relative humidity of the air, the ambient temperature, the distance and emissivity of the target using the empirical relationships provided by FLIR.

The emissivity spectrum of basalts is provided by the Arizona State University (Christensen et al., 2000) (Fig. 4). In the wavelength domain of the camera, the average emissivity is 0.95. Depending on the surface roughness, grain size, and possible contamination by other material (dust coating), this emissivity could drop down to 0.85. Thus, a value of $0.90 \pm 0.05$ was adopted in this study, leading to an uncertainty of temperature $\leq 0.5$ ° C. The relative uncertainty is expected to be considerably lower than this value, especially when comparing temperatures within the 2 Formica Leo craters where a relatively homogeneous surface of basaltic scorias is found. However, complication may arise from the effects of topography or viewing angles. Because of the angle of view of our camera, the temperatures might be affected by the non-Lambertian behavior of the surfaces (Coret et al., 2004). However the temperature variations around the cone does not appear to be related to the variations of the emergence angle in the images

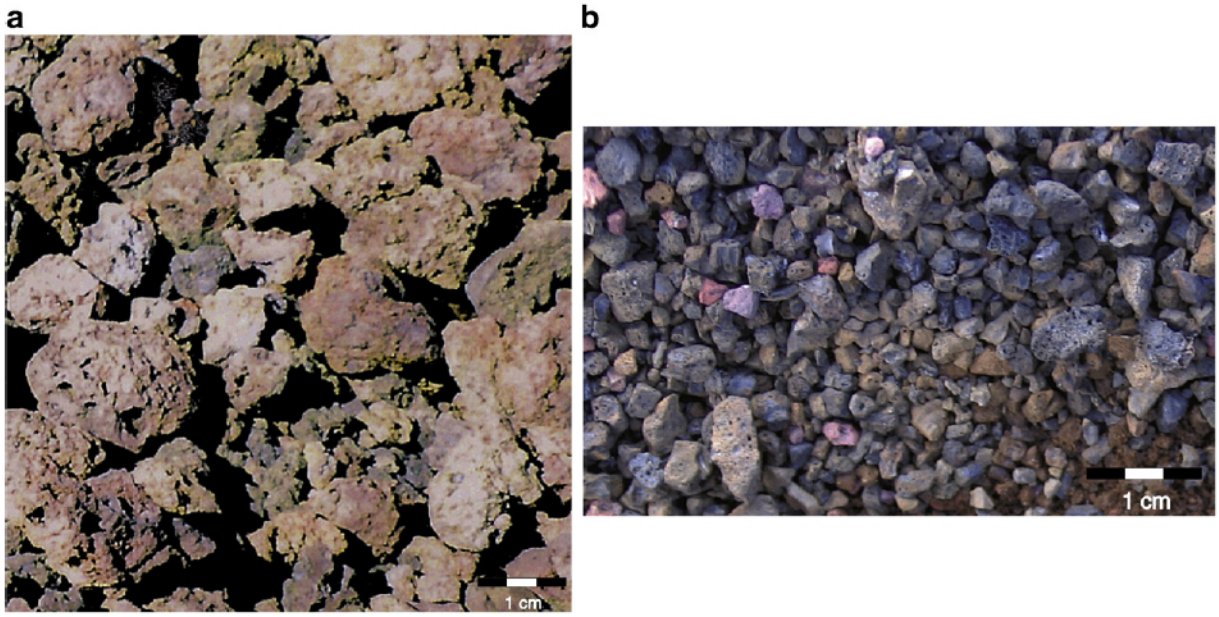


**Fig. 3.** a) View of blocks and fine lapillis found on the bottom of the SE crater (sites B and D on Fig. 2), b) View of blocks and fine lapillis found on the top of Formica Leo (sites A and C on Fig. 2).

acquired from the caldera rim, as in the 2001 helicopter flyby. The non-Lambertian behavior may still affect the estimated absolute temperatures, but such errors do not affect our application.

Finally, the resolution of the sensor is about 0.08 °C at 30 °C. Given the distance of the target, a spatial resolution of ~40 cm is obtained. 30 images have been taken at regular time intervals. Despite the efforts to maintain the camera motionless, winds induced slight offsets. Thus, a geometric correction is required to study the time evolution of the temperature at a given location. We manually selected 10 control points to register and warp each image to the first one, using a RST transformation (rotation, scaling and translation). A maximum misregistration between images of about 40 cm is estimated from the comparison of the position of some objects identified on each image (rocks, fractures, rim crests). Six of the processed images are displayed in Fig. 5. During the night, the floors of both craters of Formica Leo (B and D sites, as indicated on the Fig. 2) are cold while the rim crests are warm. The lapillis at the feet of the flanks of the cone (E site, see Fig. 2) are also cold. The surrounding massive basalts are warmer than the cone with greatest temperatures found inside fractures. As expected, during the day, the hottest regions correspond to the areas illuminated with nearly vertical incidence angles, while cold ones are in the shadow.

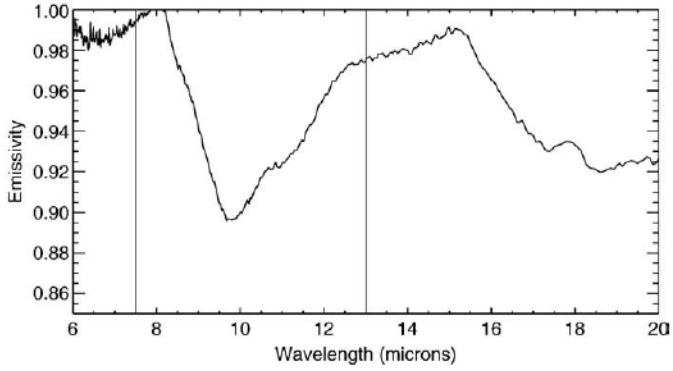


**Fig. 4.** Emissivity spectrum of basalt from the Arizona State University spectral library (sample 659, basalt substrate — clean). Vertical bars indicate the wavelength band of the thermal camera used in this study. The average emissivity in this 7.5–13 mm band is 0.95.

## 3. Comparison of observed and calculated diurnal surface temperatures assuming a flat surface

In Appendix A, we review the basic 1-D equations allowing for the diurnal temperature profile $T(z, t)$ through a volcanic vegetation-free soil ($z$ and $t$ designate the depth and time, respectively). The equation is solved with finite difference scheme that is second order in time and space for a soil layer of thickness $H_{lay} = 0.35$ m, with a spatial resolution of $3.5\ 10^{-3}$ m and time resolution of 1 min. The parameters of the model and their assumed values are summarized in Table 1. Different spots outside and within Formica Leo are studied.

### 3.1. Diurnal surface temperatures outside Formica Leo

Observed and calculated temperatures at different locations outside Formica Leo are compared (Fig. 6). To avoid difficulties arising from possible residual misregistration, the observed temperatures are averaged on surfaces of about 0.64 $m^2$ (4 pixels). Within these areas, the standard deviation of surface temperatures between 7 p.m. and 5 a.m. never exceeded 0.1 °C. During the day, fine lapillis warm up more rapidly than coarse lapillis, and a difference of $\leq 4$ °C is recorded at noon (Fig. 6). Also, coarse lapillis warm more rapidly than massive basalts. Observed profiles match calculated ones provided the following conductivity $k$ for each type of soil is chosen: 0.5 W $m^{-1}$ $K^{-1}$ for fine lapillis (5 mm), and 1.5 W $m^{-1}$ $K^{-1}$ for an intermediate surface composed of both lapillis and massive basalts and 2.5–3 W $m^{-1}$ $K^{-1}$ for massive basalts.

In order to get a direct estimate of the conductivity of a granular soil, the diurnal temperature evolution was recorded using 17 thermal probes placed at a distance $D = 15$ cm depth inside the soil of the Plaine des Sables plateau (Fig. 7) ($d = 0.5$ cm grain size). The cooling down process propagating after sunset reached the depth $D$ after about $t = 10$ h (Fig. 7). The thermal diffusivity $\kappa$ of the lapilli soil is calculated using the solution for instantaneous cooling of infinite half-space (Turcotte and Schubert, 2002):

$$\kappa = \frac{D^2}{4t} = 1.510^{-7} \mathrm{m}^2 \quad (1)$$

The volumetric heat capacity of the soil $h_s$ is approximatively equal to:

$$h_s = (1-n)\rho_b c_b \quad (2)$$

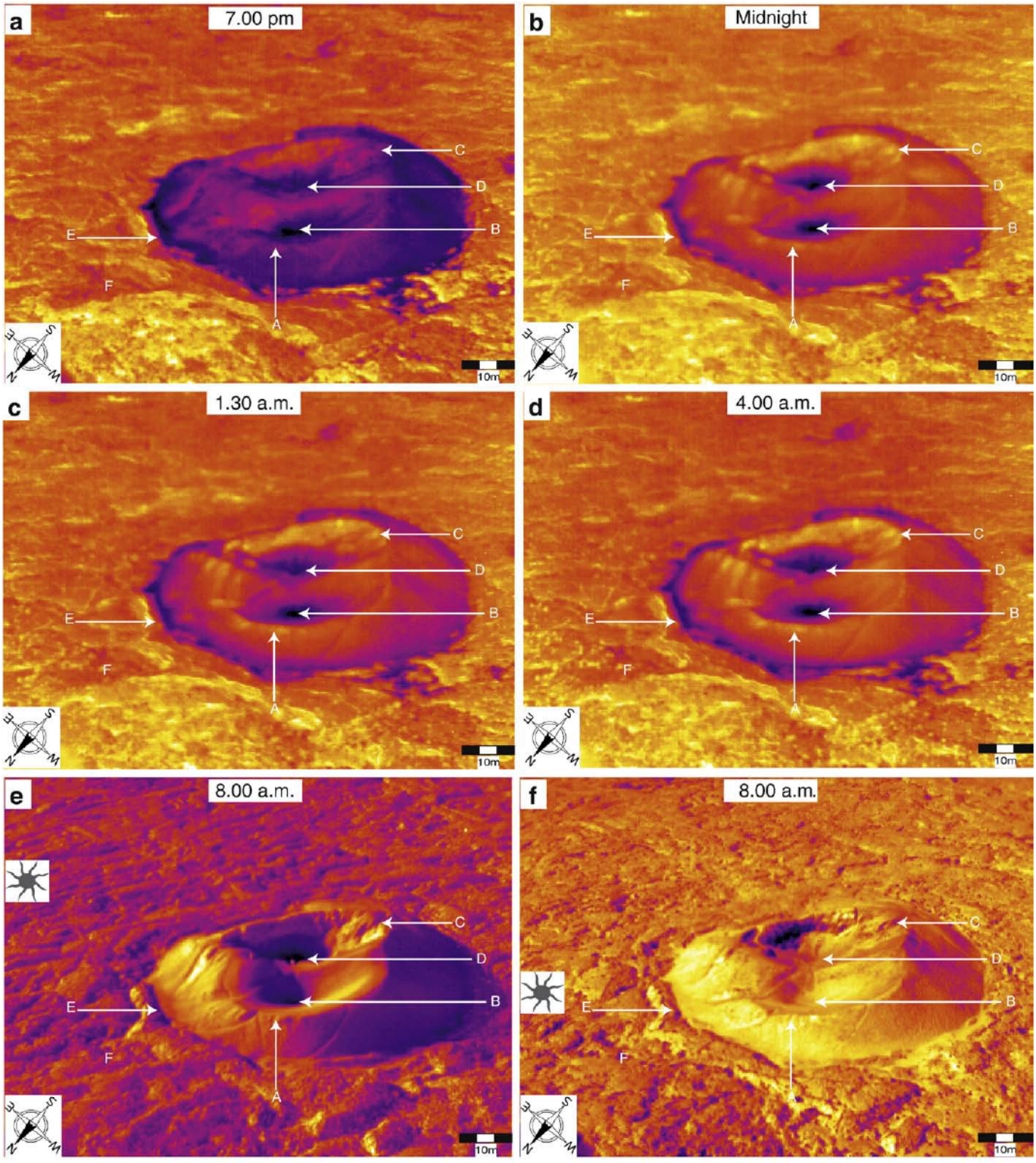


**Fig. 5.** Infrared images at different time. Bright sites are hot and dark sites are cold, arrows point at the lettered sites defined in Fig. 2b. The sun position at 8h00 a.m. and 12.00 p.m. is indicated on the daytime e and f frames.

where the terms are defined in Table 1. These relationships lead to a thermal conductivity $\kappa = 0.4\ \mathrm{W\ m^{-1}\ K^{-1}}$, i.e. a value very close to the one deduced from the radiometric data from lapilli (Fig. 6) and of (Lardy and Tabbagh, 1999) similar measurements in basaltic soils.

The soil of Formica Leo has huge variations in grain size 0.5 cm up to 15 cm. From a recent review of thermal conductivity models for granular material (Kurita et al., 2007), it appears that a good first order approximation for the effective conductivity $k$ of porous rocks and soils follow the *geometric mean model* (Woodside and Messmer, 1961):

$$k = k_a^n k_b^{n-1} \tag{3}$$

(See Table 1 for notation). This conductivity is formally independent of the grain size in this equation. Note that, if we use the values of

**Table 1**
Physical parameters related to the conductive–radiative model.

| | | |
|---|---|---|
| Thickness of the soil layer | $H_{lay}$ | 0.35 m |
| Density of the basalt | $\rho_b$ | 2700 kg m$^{-3}$ |
| Basalt specific heat constant | $c_b$ | 1000 J kg$^{-1}$ K$^{-1}$ |
| Basalt thermal conductivity | $k_b$ | 2.7 W m$^{-1}$ K$^{-1}$ |
| Soil porosity | $n$ | 0.4 |
| Soil grain size | $d$ | 0.5 cm–10 cm |
| Soil volumetric heat capacity | $h_s=\rho_b c_b$ | $2.7\times10^6$ J K$^{-1}$ m$^{-3}$ |
| Solar constant | $S_0$ | 1367 W m$^{-2}$ |
| Direct + diffuse energy fraction at the soil | $C$ | 0.5 |
| Latitude of Formica Leo | $\lambda$ | 20° S |
| Day number of the year (April, 24th) | $J$ | 113 |
| Solar declination (April, 24th) | $\delta$ | 0.2 rad |
| Emissivity | $\varepsilon$ | 0.95 |
| Stefan–Boltzman Constant | $\sigma$ | $5.67\times10^{-8}$ W m$^{-2}$ K$^{-4}$ |
| Air thermal conductivity | $k_a$ | $2\times10^{-2}$ W m$^{-1}$ K$^{-1}$ |
| Mean air temperature | $T_0$ | 281 K |
| Amplitude of the air temperature | $T_{amp}$ | 7.5 K |
| Phase shift | $t_{ph}$ | 3,600 s |
| Duration of the diurnal cycle | $P_{dc}$ | 86,400 s |

$k_a$ and $k_b$ given in Table 1 along with a porosity of 0.4, we obtain a value $k=0.4$ W m$^{-1}$ K$^{-1}$ in agreement with the estimate above.

### 3.2. Surface temperatures inside Formica Leo

During the night, the center of each crater is cold while the rim is warm (Fig. 5a to d). Infrared temperatures at midnight along profiles Tr1 and Tr2 across SE and NW craters are displayed in Fig. 8a and b, respectively. The locations of each profile are shown in the Fig. 5b. In both cases, a temperature drop of about 4 K from the rim crest toward the crater center is observed. Evolution of the infrared surface temperatures from 7 p.m. to 11 a.m. at A and B, C and D sites (see Fig. 2b for the location of the areas) are shown on Fig. 9a and b. Diurnal evolution of the infrared surface temperatures on the rim of the NW crater (A site) is compared to that of the flat coarse lapilli floor (E) and massive basalt (F) outside the cone in Fig. 9c and d. From 9 p.m. to 2 a.m., the fine lapillis along the rim become progressively warmer than the coarse lapillis at the centers and even hotter than the massive basalts surrounding the cones. These temperature patterns could result from a rim to center thermal conductivity drop. The slopes of the craters and their centers are covered with coarse lapillis (5 cm), and aggregates of vesiculated rocks up to 10–15 cm in size, respectively, with a porosity similar to that of the fine lapillis found at the rim crest. The fraction of the porosity corresponding to the vesicules should not inhibit significantly the effective thermal conductivity of the soil (Kurita et al., 2007). Thus, there is no reason for the rocks found at the craters centers to have a significantly lower thermal conductivity that the fine lapillis. Moreover, the contacts between fine, coarse lapillis and blocks are well-marked on Formica Leo. If the thermal patterns inside the craters corresponded to thermal conductivity variations, strong temperature contrasts between the different lithologies should be observed along Tr1 and Tr2 profiles, which is not the case. The present radiative-conducitve modeling valid for flat surfaces should be modified to explore the effects of the local topography.

## 4. Influence of the cone topography on the diurnal surface temperatures

In the craters, a portion of flank exchanges energy with the sky and with others flanks in the upper hemisphere ($2\pi$ solid angle). Neglecting absorption and diffusion in the atmosphere, face to face surfaces with the same temperature have a zero net radiative balance. During the night, the surface temperature contrast along the different faces of the cones is small as all flanks of Formica Leo receive the same amount of solar energy during the day. This implies that the thermal budget between the flanks is negligible. The cooling of the flank is controlled by the radiative exchange with the fraction of the sky seen from that portion of the flank (Whiteman et al., 1989, 2000). This situation decreases the rate of energy loss $E(x)$ along all the slopes of the cones in comparison to that of a flat surface (Fig. 10):

$$E(x) = p(x)\epsilon\sigma T^4 \tag{4}$$

where $p$ is the fraction of sky seen at the distance $x$ of the rim. We approximate the sky fraction $p(x)$ by $\alpha(x)/\pi$ where $\alpha(x)$ is the angle between each rim evaluated at each point of the flank (Fig. 10). From the rim down to the center of the SE crater, $p$ decreases from 1 to 0.63 (cf. Fig. 10). The 1-D calculation of surface temperatures is done taking into account the variable rate of energy loss along a radial profile of the cone. Atmospheric radiations are also taken into account and are described in Appendix A, assuming a thermal conductivity of 0.4 W m$^{-1}$ K$^{-1}$ (Section 1). The calculated temperature at midnight is compared with those measured along Tr1 (Fig. 11). The rim to crater center drop $p$ induces a non linear increase in surface temperature (Eq. (4)), which reaches 20 °C in the crater center. This is opposite to the observations (Fig. 11).

## 5. Convection model inside Formica Leo: the slope effect

### 5.1. Additional field observations suggesting air convection

In the previous sections, we have shown that the observed temperatures inside Formica Leo cannot be explained neither by a contrast of thermal conductivity associated with a difference of lithology in the cone nor by the radiative effects associated with topography. Other thermal processes have been searched to explain field observations but negative conclusions have been obtained for the two following alternative hypotheses. i) Water evaporation could extract heat from the center of the cone, cooling it. Humidity measurements show that during the night, air is saturated with water vapor (97–98% relative humidity). Then, we do not see the reason why evaporation could differentially extract heat from some areas of the soil of the cone with a homogeneous saturated atmosphere above it. ii) The presence of nighttime irregular fog at the center of the cone could also affect the thermal image. However, the atmosphere was perfectly clear in several cases for which the temperature contrast is observed. Fog,

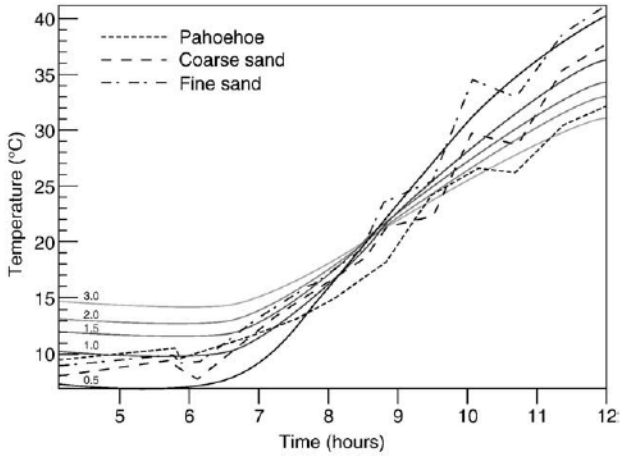


**Fig. 6.** Observed and calculated surface temperatures from 4 a.m. to noon at three locations on the plateau outside Formica Leo. Dotted lines are infrared temperatures on fine, coarse lapillis and massive basalt soils (E and F sites). The calculated profiles are for the thermal conductivities of the porous basalt layer ranging from 0.5 W m$^{-1}$ K$^{-1}$ (black line) to 3 W m$^{-1}$ K$^{-1}$ (light-grey line). The lower values of conductivity match the observations for the fine and coarse lapilli soils while the higher ones match the massive basalt.

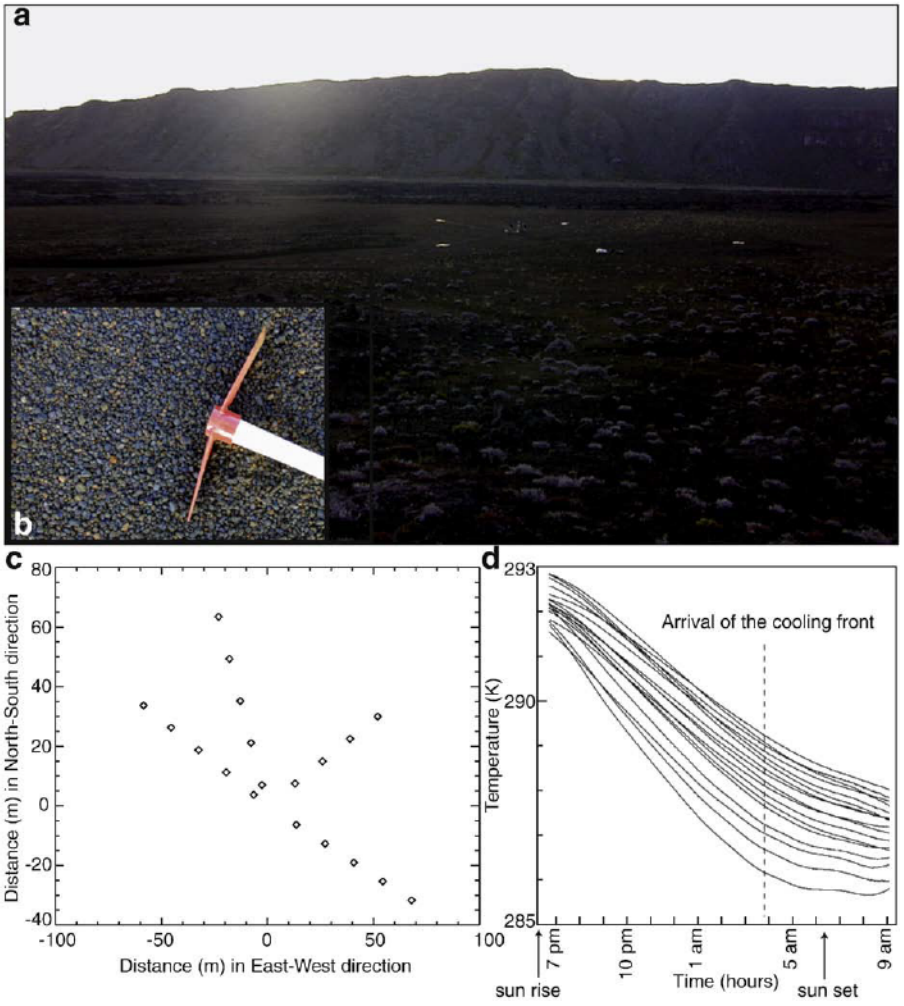


**Fig. 7.** a) Picture of the thermal probes installed at the Plaine des Sables plateau; b) Plaine des sables typical granular size (grain size $d \approx 5$ mm).; c) Field map of the 17 thermal sensors (PT100 probes); d) Time evolution of the temperatures measured by the sensors at depth D = 15 cm.

when present, is not responsible for the rim crest to crater center temperature drop.

Having reviewed all thermal processes that could affect the surface temperatures at Formica Leo, we believe that the only way to explain the observed thermal profiles is air convection. This idea is also suggested by several other field observations. On the morning following our April 25th nighttime infrared measurements, an anemometer (Campbell Scientific anemometer) placed 10 cm above the

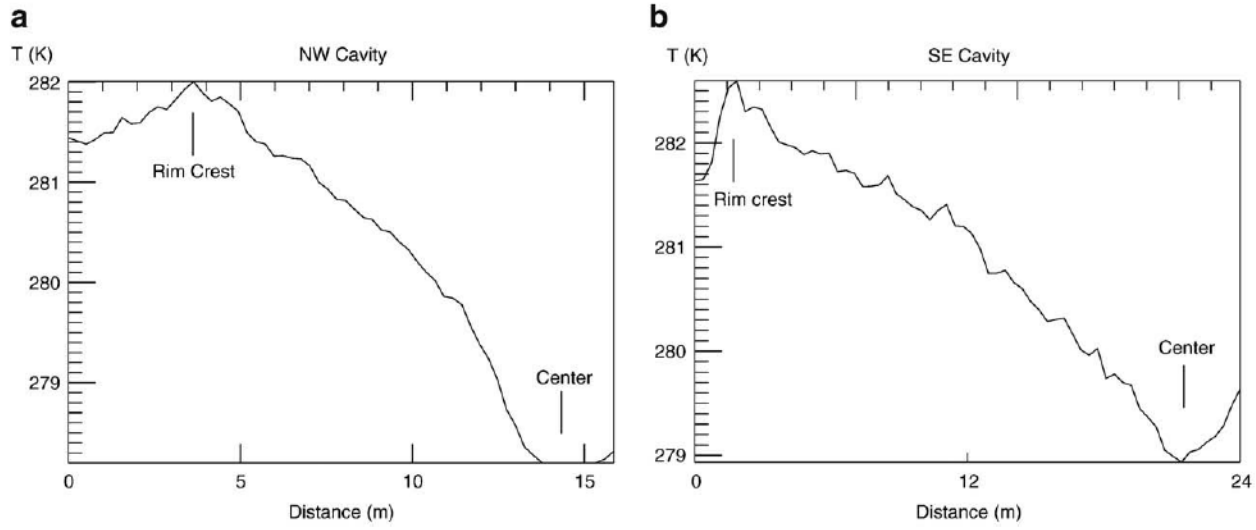


**Fig. 8.** Infrared surface temperature at midnight along Tr1 and Tr2 transects, respectively (see Fig. 5b for transects locations).

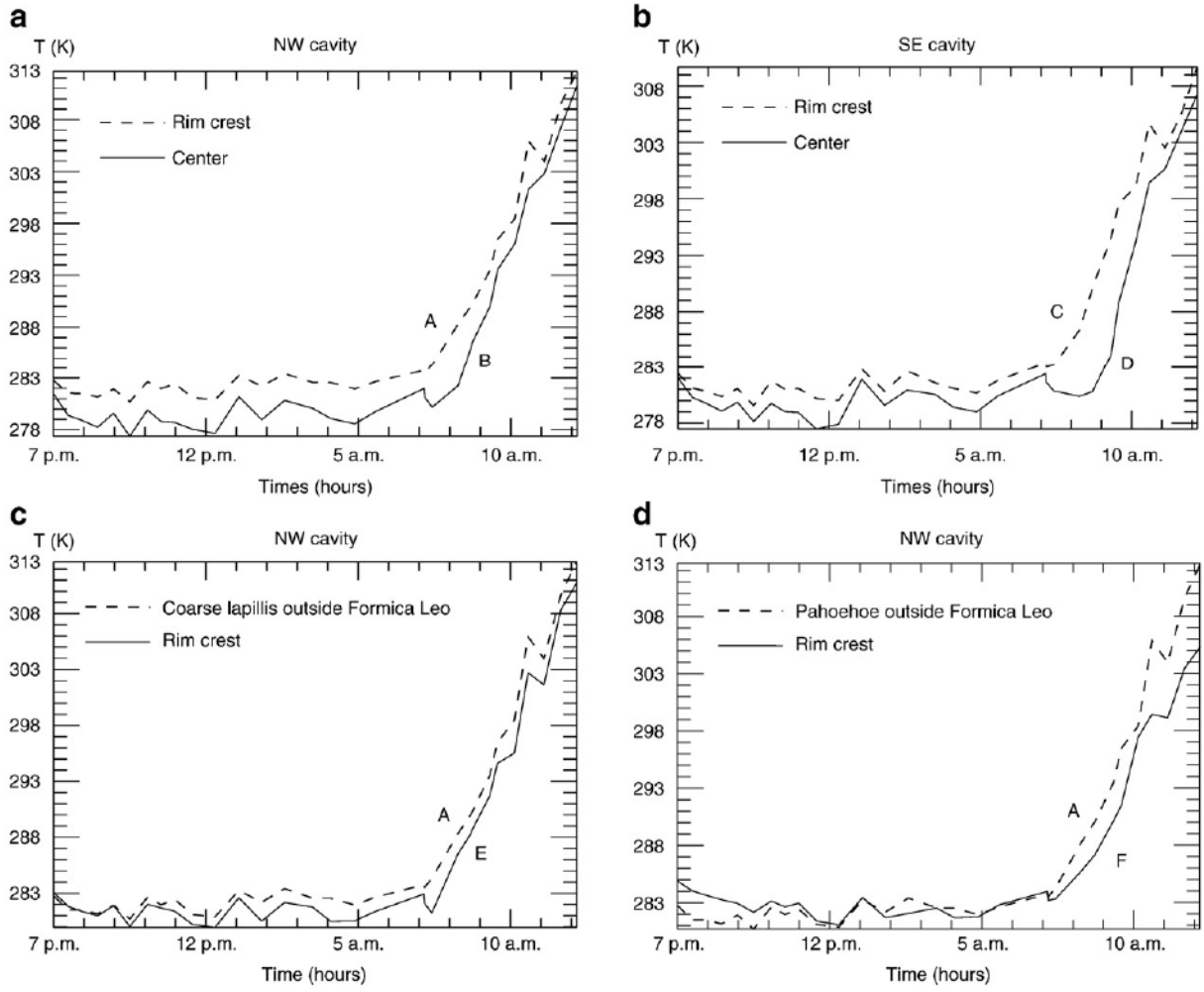


**Fig. 9.** Time evolution of surface temperatures; (a) dashed and solid curves represent the temperature at the rim and at the center of the NW crater of Formica Leo (A, B sites), respectively; (b) similar temperature profiles on the SE crater (C,D sites); (c) temperatures on the rim of the NW crater (A site) and on the coarse lapillis floor outside the cone (E site); (d) Temperatures on the rim (D site) and on the massive basalt outside the cone (F site).

crater center detected air speed as low as 20 cm $s^{-1}$. When the propellers were parallel to the surface, they rotated fast, while the motion was much slower when they were placed perpendicularly to the surface. This direct observation indicates the presence of an air flow with a dipping component much stronger than the horizontal one inside the highly permeable soil. It constitutes an important independent observation in favor of air convection within Formica Leo craters. This strong vertical component of the air flow was specific to the crater center and nothing comparable was seen elsewhere, in particular at the rim of the cone. Another direct evidence of air convection was obtained in August 2007. A 30 cm depth temperature profile across the SE crater was measured using 30 thermal probes and a digital thermometer (Fig. 12). This profile displays a rim to crater center temperature drop of about 6 °C. Such subsurface temperature variations can be explained only assuming a convective air flow. In the following, a physical model for the air flow inside the cone is presented and the possibility of convection depending mainly on permeability is explored by numerical simulations.

### 5.2. The equations of air convection

Numerous experimental and numerical studies consider the convection of water in inclined porous layers (Boriès and Combarnous, 1972; Wood and Hewett, 1982; Caltagirone and Boriès, 1985; Rosenberg et al., 1993; Chevalier et al., 1998; Baytas and Pop, 1999; Rabinowicz et al., 1999; Zhao et al., 2004; Zhang et al., 2005).

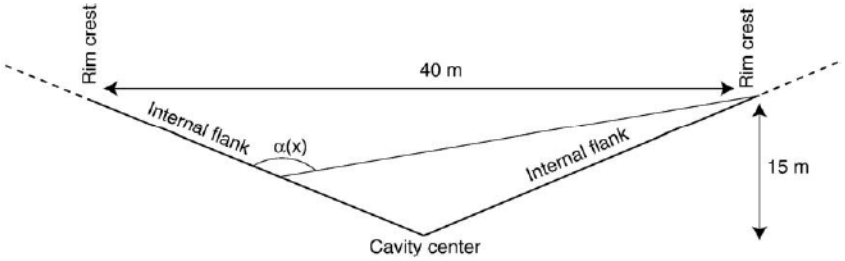


**Fig. 10.** Sketch of Formica Leo craters and geometric parameters for the calculation of the sky proportion $p$ (see Eq.).

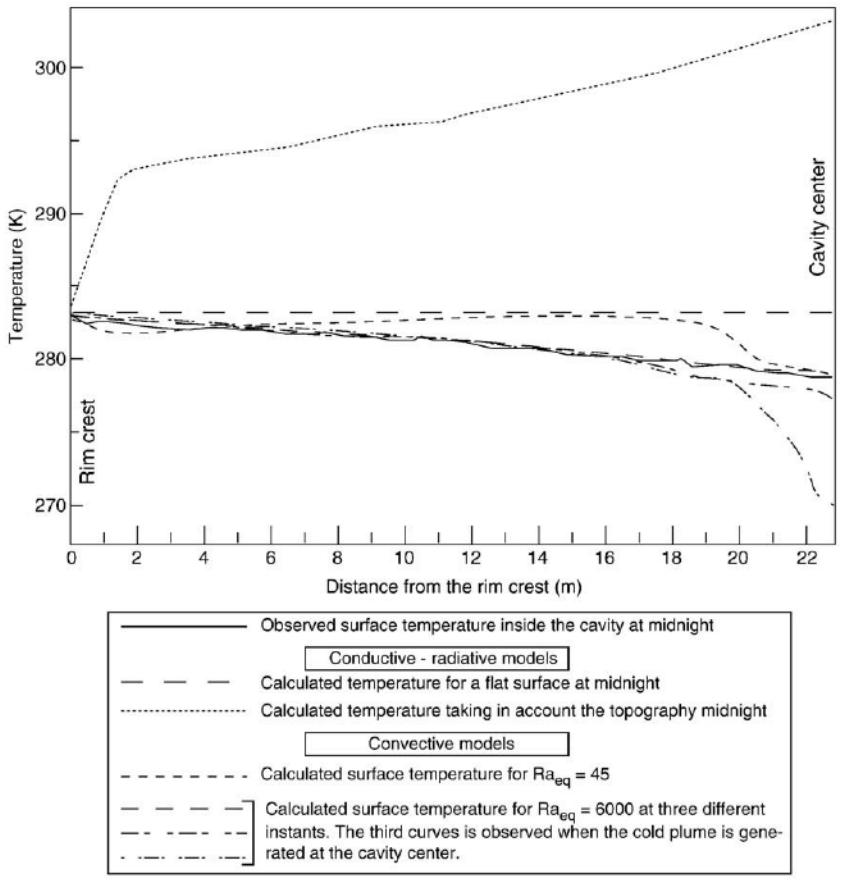


**Fig. 11.** Comparison of the infrared temperature profile across SE crater of Formica Leo at midnight for the conductive–radiative models with flat and sloped surfaces, and for the convective models.

Numerical and experimental works have been done on convection of air in subarctic soils to study its influence on avalanches of snow (Sturm, 1991; Sturm and Johnson, 1991). Others have done laboratory (Yu et al., 2005) and numerical (Zhang et al., 2005) investigations on rock cooling by air convection in permafrosts for railway/roadway engineering purposes. Rose and Guo (1995) conducted numerical studies of thermal convection of air in sloped soils. No previous work reports on air convection within sloped ventilated volcanic systems whose surface temperature evolves during day and night. Our objective is to explain surface temperatures across Formica Leo just before the dawn, when the surface temperature is a minimum, and the effect of illumination angles and topography are negligible. We use a 2-dimensional code already developed in our laboratory (Rabinowicz et al., 1999). The mathematical development of the 2-dimensional porous flow convection is based on the following standard equations. The equation of mass conservation is:

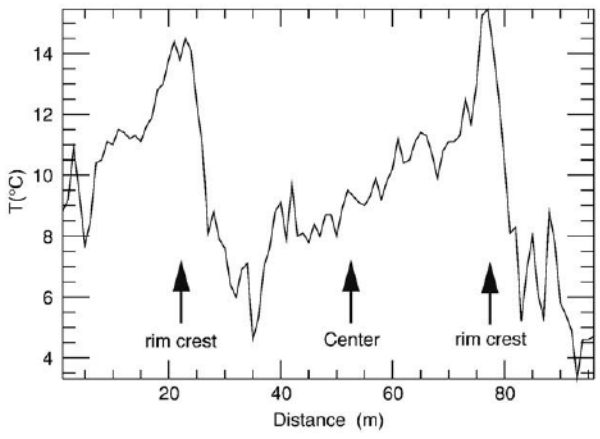


**Fig. 12.** Temperature profile at the largest crater of Formica Leo and at 0.3 cm depth. The temperature profile was acquired between 3 p.m. and 5 p.m. The large temperature variations can be only explained by the occurrence of convection cells with cold air entering the center of the crater and warm air exiting through the rims.

$$\vec{\nabla} \cdot \vec{q} = 0 \tag{5}$$

where $\vec{q}$ is the Darcy velocity which represents the product of the air velocity $\vec{v}$ in the porous medium with the porosity $n$ of the rock $\left(\vec{q} = n\vec{v}\right)$. We write the Darcy's equation:

$$\frac{\partial P}{\partial x} + g\rho_a \sin\phi - u\frac{\mu}{K} = 0 \tag{6}$$

$$\frac{\partial P}{\partial z} + g\rho_a \cos\phi - w\frac{\mu}{K} = 0 \tag{7}$$

where $u$ and $w$ are the Darcy velocities projected along the $x$ and $z$ directions which are parallel and orthogonal to the slope of the porous layer, respectively ($z$ points downward, cf. Fig. 13). The angle of the porous layer with respect to the horizontal direction is $\phi$. $P$ is the gas pressure, $g$ is the gravity, $\rho_a$ and $\mu$ are the density and the dynamical viscosity of the air, respectively. The heat transfer equation is:

$$(1-n)\rho_b C_b \frac{\partial T}{\partial t} + n\rho_a C_a\left(u\frac{\partial T}{\partial x} + w\frac{\partial T}{\partial z}\right) = \kappa\vec{\nabla}^2 T \tag{8}$$

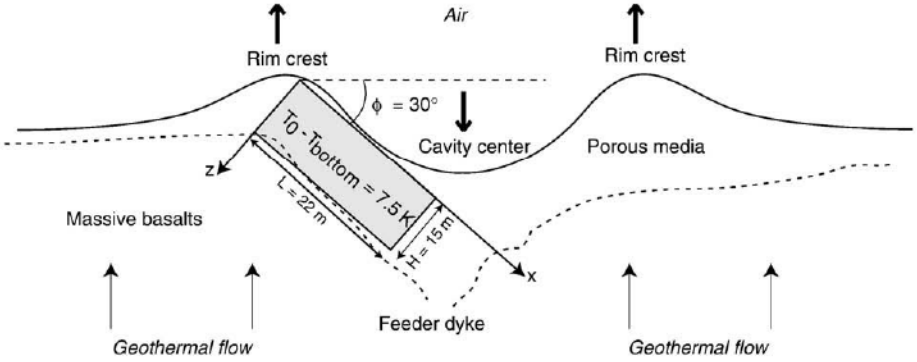


**Fig. 13.** Representation of the inclined box used to model air convection within Formica Leo.

where $C_a$ is the heat capacity of the fluid. Dividing both sides of the equation by the soil volumic heat capacity $(1-n)\,\rho_b C_b$, the equation becomes:

$$\frac{\partial T}{\partial t} + \gamma\left(u\frac{\partial T}{\partial x} + w\frac{\partial T}{\partial z}\right) = \kappa\vec{\nabla}^2 T \tag{9}$$

where $\gamma$ is the air-soil volumic heat capacity ratio:

$$\gamma = \frac{\rho_a c_a n}{\rho_b c_b (1-n)} \tag{10}$$

In the numerical code, $\gamma u$ and $\gamma w$ are related to the stream function by:

$$\gamma u = \frac{\partial \psi}{\partial z} \tag{11}$$

$$\gamma w = -\frac{\partial \psi}{\partial x} \tag{12}$$

These equations apply to an incompressible air flow which is slow enough for the temperature of the air and the solid fraction of the porous media to be the same. The incompressibility is easily verified: the excess pressure during air convection in soils is negligible in comparison to the hydrostatic pressure. Because of the slow rate of the temperature variations with time in the soil (see below) the air and soil are likely in equilibrium all times. We used the following equation of state for the air density:

$$\rho_a = \rho_0(1 - \alpha(T - T_0)) \tag{13}$$

where $\rho_0$ and $\alpha$ are respectively the density of the air and the thermal expansion coefficient at the mean temperature $T_0$. The non-dimensional temperature ($\overline{T}$), the stream function $\overline{\psi}$, the distances ($\overline{x}$ and $\overline{z}$), velocities ($\overline{u}$ and $\overline{w}$), and time ($\tau$) are introduced using the following scaling:

$$T - T_0 = \Delta T^* \overline{T} \tag{14}$$

$$x = H\overline{x} \tag{15}$$

$$z = H\overline{z} \tag{16}$$

$$\psi = \kappa\overline{\psi} \tag{17}$$

$$\gamma u = \frac{\kappa}{H}\overline{u} \tag{18}$$

$$\gamma w = \frac{\kappa}{H}\overline{w} \tag{19}$$

$$t = \frac{H^2}{\kappa}\tau \tag{20}$$

where $H$ is the layer thickness, $\Delta T = T_{bottom} - T_0 = 7.5$ K and $T_{bottom} = 288.5$ K is the temperature at the bottom of the soil layer. Assuming that the viscosity $\mu$, the permeability $K$ and the thermal expansion coefficient $\alpha$ are constant, the equations of convection become:

$$\frac{\partial \overline{T}}{\partial \tau} + \left(\overline{u}\frac{\partial \overline{T}}{\partial \overline{x}} + \overline{w}\frac{\partial \overline{T}}{\partial \overline{z}}\right) = \vec{\nabla}^2 \overline{T} \tag{21}$$

and

$$\vec{\nabla}^2 \overline{\psi} = -\gamma Ra\left(\frac{\partial \overline{T}}{\partial \overline{x}}\cos\phi - \frac{\partial \overline{T}}{\partial \overline{z}}\sin\phi\right) \tag{22}$$

where $Ra$ is the Rayleigh number:

$$Ra = \frac{\rho_0 g \alpha \Delta T H K}{\mu\kappa} \tag{23}$$

In the case of water porous flow, the volumetric heat capacity of the water $\rho_w\, c_w$ is approximately that of the basalt. With $\gamma \approx 1$ (Cherkaoui and Wilcock, 1999), the above dimensionless equations are similar than those describing convection of water. However, the air has a volumetric heat capacity which is over 3 orders of magnitude less than that of the rock ($\gamma = 5.0\times10^{-4}$). In consequence, the heat transported by the air is large in comparison with conducted heat at the condition that the Darcy velocity of the air is extremely high. This is the reason why air convection is generally not considered in modelling the transport of heat through volcanic structures. However, we show below that air convection can transport significant heat in the soil of Formica Leo craters because of their high permeability and high associated velocities.

**Table 2**
Notation and values of the physical parameters used for the convective model.

| | | |
|---|---|---|
| Height of the box | $H$ | 15 m |
| Length of the box | $L$ | 22 m |
| Slope of the box | $\phi$ | 30° |
| Heat capacity of the air | $C_a$ | 1000 J kg$^{-1}$ K$^{-1}$ |
| Air density | $\rho_a$ | 1 kg m$^{-3}$ |
| Air thermal expansion | $\alpha$ | $3.7\times10^{-3}$ K$^{-1}$ |
| Air Viscosity | $\mu$ | $1.5\times10^{-5}$ Pa s |
| Air–soil volumic heat capacity ratio | $\gamma$ | $5.0\times10^{-4}$ |
| Permeability of the soil | $K$ | $3\times10^{-8}$–$10^{-5}$ m$^2$ |
| Thermal conductivity of the soil | $k$ | 0.4 W m$^{-1}$ K$^{-1}$ |
| Porosity of the soil | $n$ | 0.4 |
| Top to bottom temperature contrast | $\Delta T$ | 7.5 K |
| Phase shift | $\zeta$ | 0 |
| Pulsation scale | $\Omega$ | 45,507 s |
| Darcy velocity scale | $v$ | $2.7\times10^{-5}$ m s$^{-1}$ |
| Geothermal heat flux(for $k=2.5$) | | 1250 mW m$^{-2}$ |
| Equivalent Rayleigh number | $Ra_{eq}$ | 20.4–6800 |

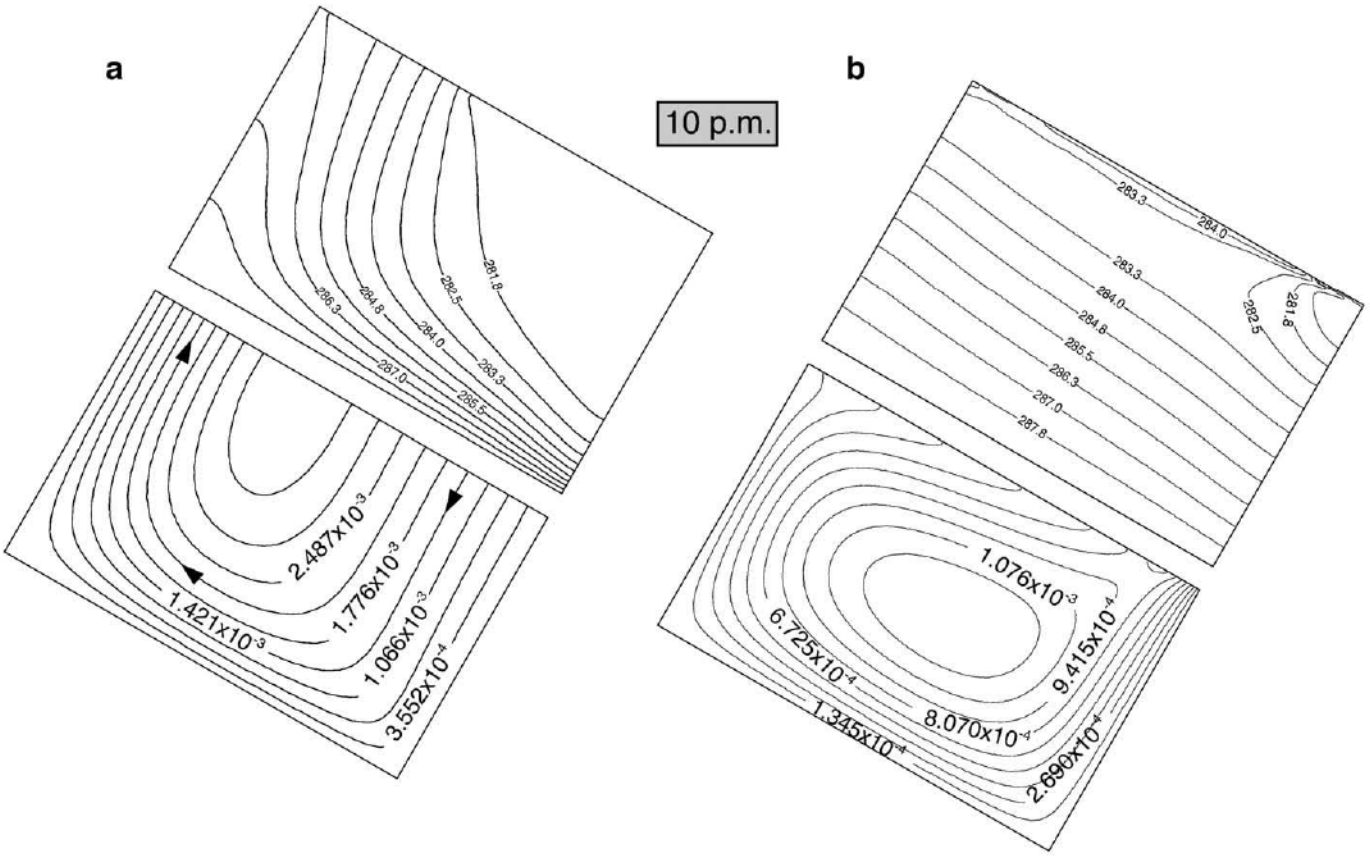


**Fig. 14.** Comparison of isotherms (in degree K) and stream lines $\psi$ (in $m^2\ s^{-1}$) for a model with an equivalent Rayleigh number $Ra_{eq}$ of 45 with a (a) constant top temperature and (b) with a fluctuating surface temperature (b); (a) represents the steady solution and (b) is the snapshot at 10 p.m. Since $\psi = 0$ on the border of the cell, the value of the streamline represents the flow rate between the border of the box and this streamline. Note that the flow rate within the convective cell is much lower when the surface temperature fluctuates (b) than when it is constant (a).

### 5.3. Parameter values and boundary conditions of the model

The vigor of air convection within the porous media is characterized with the equivalent Rayleigh number $Ra_{eq} = \gamma\ Ra$. The temperature Eq. (21) is solved with an alternative direction implicit finite difference method (Douglas and Rachford, 1956) tested for various convective problems (Rabinowicz et al., 1993; Ormond et al., 1995; Rabinowicz et al., 1999). The flow equation is solved using a spectral decomposition (Rabinowicz et al., 1999). We simulate the air flow and the temperature of the media within a rectangular sloped box representing the flank of craters (Fig. 13). The porous media has an open top permitting free circulation of the air ($\partial\bar{\psi}/\partial\bar{z} = 0$), its bottom is impervious ($\bar{\psi} = 0$). The sides are adiabatic ($\partial\bar{T}/\partial\bar{x}$) and impervious ($\bar{\psi} = 0$). The air temperature at the surface is given by:

$$\bar{T}(\bar{x}, \bar{z} = 0) = T_0 + \Delta T \sin(\Omega\tau + \zeta) \tag{24}$$

where $T_0 = 281$ K, $\Delta T = 7.5$ K and $\tau$ is the time. $\zeta$ is the phase shift and $\Omega$ is the diurnal pulsation scale:

$$\Omega = \frac{2\Pi}{P_{dc}} \frac{H^2}{\kappa} \tag{25}$$

$\Omega$ and $\zeta$ are set to have a maximum temperature of 288.5 K at 6 p.m. ($\bar{T} = 1$) and a minimum temperature of 273.5 K at 6 a.m. ($\bar{T} = -1$) (Fig. 13, Table 2). As radiative processes at the surface are approximated using a sinusoidal function, the temperature profile within the thermal skin depth is expected to be different from the one given by the convective model. Some uncertainties remain when comparing the results of the model and the observations from the infrared camera which only has access to the surface temperature.

For advection across the upper boundary, the temperature of the entering air is that of the atmosphere, while the temperature of the exiting air is that at the grid point immediately below the surface. The use of this boundary condition is essential for correct modelling of the convection (Cherkaoui and Wilcock, 1999). The numerical experiments are initialized with a 1-D conductive temperature solution with $T_0 = 281\ K$ at the top of the box and of $T_{bottom} = 288.5\ K$ at its bottom.

Table 2 shows the different values of the parameters and physical constants used. We assume that the bottom of the box representing the interface between massive basalts and soil is parallel to the sloped surface (Fig. 13). As a result, the approximative thickness $H$ of the soil throughout Formica Leo is 15 m. Outside the cone, the soil being indurated has a conductivity $k$ of about 2.5 W $m^{-1}$ $K^{-1}$ (Section 1). The assumption predicts the conductive heat flux in the volcano $k\Delta T/H = 1250$ mW $m^{-2}$. This value is reasonable for a volcano with a magmatic chamber lying between about 1 and 2 km depth (Rabinowicz et al., 1998).

**Fig. 15.** Time evolution of isotherms (in degree K) and stream lines (in $m^2\ s^{-1}$) during 63 h for the model with an effective Rayleigh number $Ra_{eq}$ of 45 and a fluctuating surface temperature (see Fig. 14b).

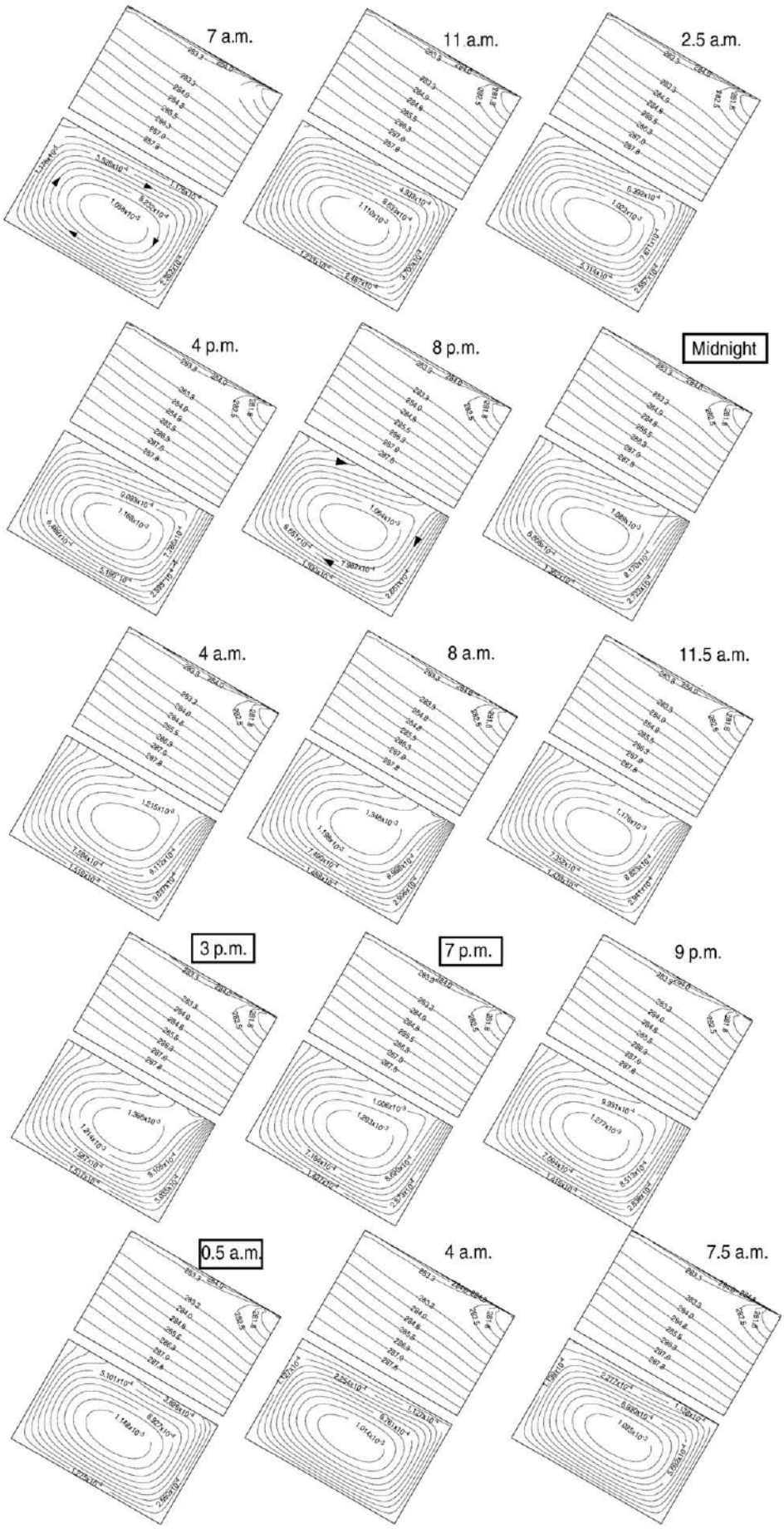
7 a.m.
11 a.m.
2.5 a.m.
4 p.m.
8 p.m.
Midnight
4 a.m.
8 a.m.
11.5 a.m.
3 p.m.
7 p.m.
9 p.m.
0.5 a.m.
4 a.m.
7.5 a.m.

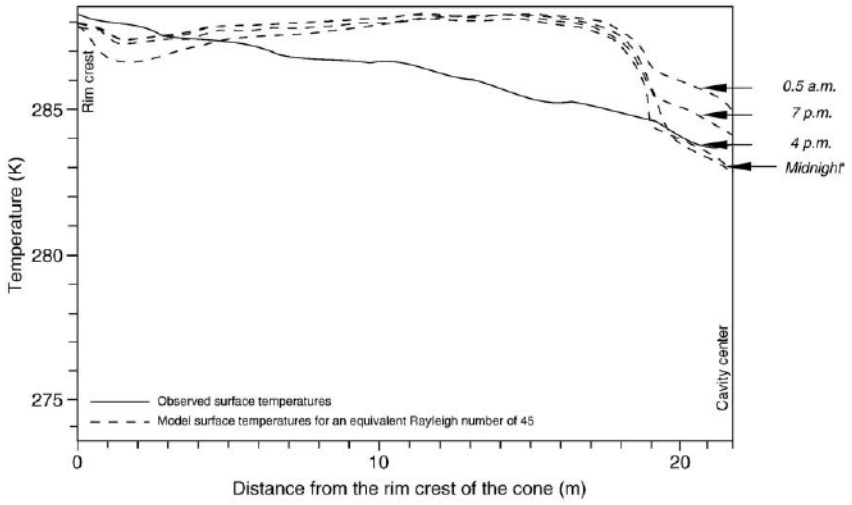


**Fig. 16.** Surface temperatures of the convective model with an equivalent Rayleigh number $Ra_{eq}=45$ at different times (dotted lines). For comparison, the observed surface temperature (plain line) at midnight along the SE crater is displayed (Tr1 transect, see Figs. 5b and 11).

The permeability $K$ is estimated from Kozeny–Carman equation (Carman, 1961):

$$K = \frac{n^3 d^2}{(1-n)^2 * 172.8} \tag{26}$$

The soil filling the central parts of the craters is particularly coarse ($d \approx 5$ to 10 cm). A straight application of Kozeny–Carman's permeability law leads to $K$ values ranging from $3.10^{-6}$ m$^2$ to $10^{-5}$ m$^2$. However, this law supposes that the space between aggregates is filled with air. It is likely that Formica Leo aggregates are partially filled with Plaine des Sables type of lapilli. The size of the grains composing this soil are relatively small ($d \approx 5$ mm), leading to a permeability $K$ of $3\times10^{-8}$ m$^2$. Thus, the permeability of the soil can be reasonably bounded by $K=3\times10^{-8}$ m$^2$ to $10^{-5}$ m$^2$. Within this range of permeability, the equivalent Rayleigh number $Ra_{eq}$ ranges from 20 to 6800, a value generally above the critical value for convection in a horizontal layer 27.1, (Cherkaoui and Wilcock, 1999). Thus, air convection should occur within Formica Leo. Measured permeability of the Piton de la Fournaise massive basalt yields a value of about $3.10^{-11}$ m$^2$ (Fontaine et al., 2002). With this permeability, the equivalent Rayleigh number $Ra_{eq}=\gamma\ Ra$ of water saturated media is close to critical value for convection. Assuming the permeabilities estimated at Formica Leo ($3\times10^{-8}$–$10^{-5}$ m$^2$), the equivalent Rayleigh number ranges from 1000 to $3\times10^5$. For the highest permeabilities values (preferred here, see below) we can expect the convective water flow to be highly turbulent with a quasi constant subsurface temperature (Caltagirone and Boriès, 1985). In such case, constant temperatures through Formica Leo would be observed, in contradictions with our IR data. In most volcanoes, highly permeable soils are likely saturated with water and will not be able to sustain the rim to crater center radiometric temperature drop we observe at Formica Leo.

### *5.4. Air convection with a Rayleigh number of 45 and a constant temperature prescribed at the surface*

Fig. 14a displays the asymptotic steady flow obtained when the effective Rayleigh number $Ra_{eq}$ is 45 and the surface temperature is arbitrarily supposed to remain equal to the mean air surface temperature $T_0=281$ K during the whole diurnal cycle. A unique cell develops: the air enters the box at the center of the cone and exits it at the rim crest. The exit temperature has a parabolic shape decreasing from 286 K at the rim down to 281 K at mid-flanks (Fig. 14). The entrance Darcy velocity at the crater center is about 0.5 mm s$^{-1}$. Thus, the heat is advected at a velocity ($\gamma u$, $\gamma w$) equal to about 1 mm h$^{-1}$ because $\gamma=5\times10^{-4}$ (see Eq. (9)). After 1 h, this velocity is small enough for the air temperature to equilibrate with 1 cm grains. The isotherms obtained with an effective Rayleigh number of 20 (not shown here) are strictly parallel to the slope. This confirms that, whatever the Rayleigh number, convection occurs in an inclined layer. However, convection transports sufficient heat in order to deform the isotherms from the conductive solution only when the effective Rayleigh $Ra_{eq}$ is above the critical value for the horizontal case (27.1).

### *5.5. Air convection with a Rayleigh number of 45 and a surface temperature following the diurnal cycle*

Figs. 14b and 15 display the 3 days transient evolution of convection with an equivalent Rayleigh number $Ra_{eq}$ of 45 and a 7.5 K oscillating surface temperature oscillating. The experiment starts with the temperature field obtained from a preliminary run lasting several years, during which the temperature reaches quasi-asymptotic regime, at which the mean heat flux is stabilized. Three striking observations are reported: (1) no steady motion is reached, (2) the fluctuations of the isotherms with time are not compatible with a daily cycle, (3) convection exhibits two different patterns: during some periods, the convective cell is entirely confined within the box; at other periods air enters the box at the crater center and exits it at the rim crest. The cell is confined in the box for ≈15 h and opens during about 45 h.

We note the development of a thick thermal convective boundary layer. It develops because of the transient confinement of the air flow. The opening and closing of the convective cell is not compatible with a daily cycle because it depends on the physics of the thermal boundary layer. We note that the convective circulation is much slower and that the lateral gradients of temperature are much less steep than the ones found with a constant surface temperature model (cf. comparison between Fig. 14a and b). Strikingly, the temperature field in the lower half of the box remains steady, while the temperature in the very shallow subsurface below the crater center is alternatively warm and cold. Fig. 16 shows temperature profiles at different times. Then, the crater center displays a temperature difference with that of the rim crest of ≈4 K and 6 K when the box is closed and opened, respectively.

**Fig. 17.** Isotherms (in K) and stream lines (in m$^2$ s$^{-1}$) of the convective porous flow over 30 h for a model with an equivalent Rayleigh number $Ra_{eq}$ of 6000 and a fluctuating top temperature. The frames indicate the time of the profiles obtained in Fig. 18.

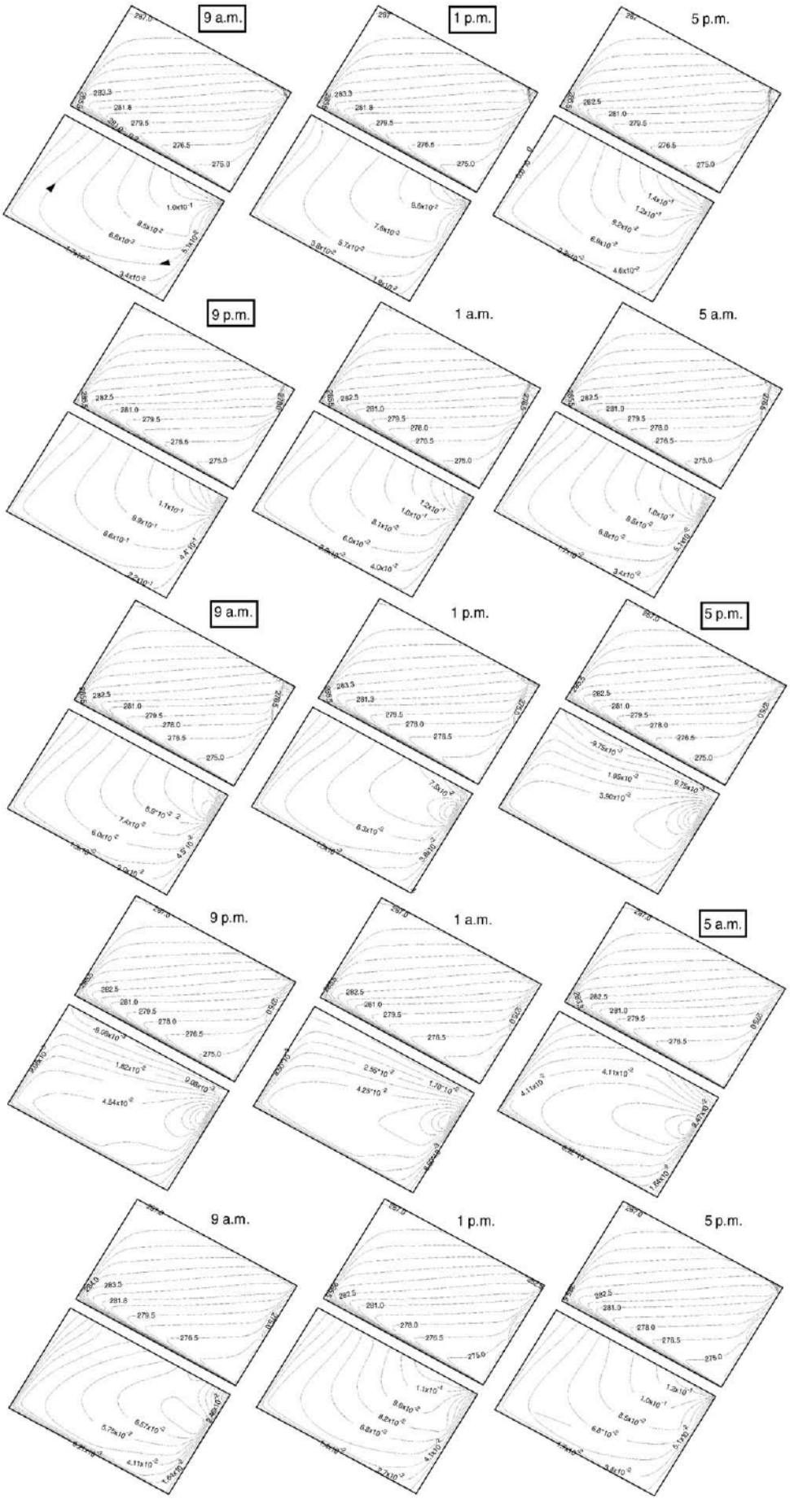
9 a.m.
1 p.m.
5 p.m.
9 p.m.
1 a.m.
5 a.m.
9 a.m.
1 p.m.
5 p.m.
9 p.m.
1 a.m.
5 a.m.
9 a.m.
1 p.m.
5 p.m.

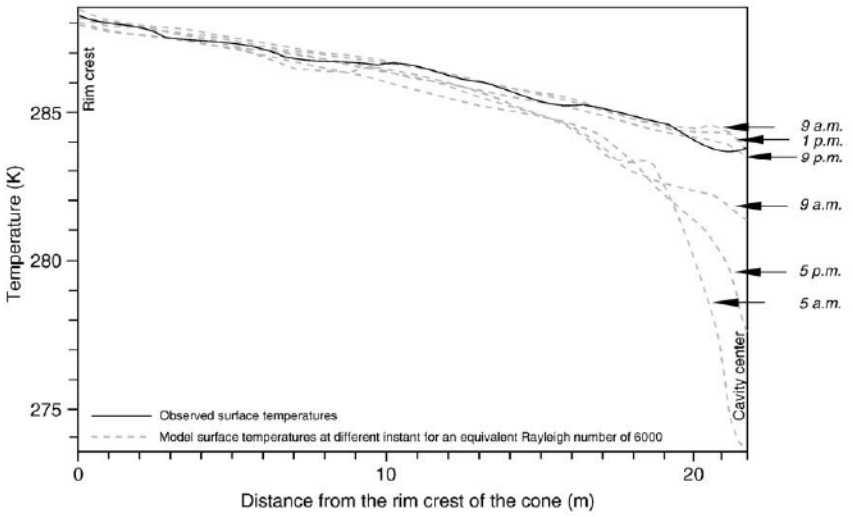


**Fig. 18.** Surface temperatures of the convective model with an equivalent Rayleigh number $Ra_{eq} = 6000$ at different times (dotted lines). For comparison, the observed surface temperature (plain line) at midnight along the SE crater is displayed (Tr1 transect, see Figs. 5b and 11).

*5.5.1. Air convection with a Rayleigh number of 6000 and a surface temperature following the diurnal cycle*

Fig. 17 displays a 30 h transient evolution of the convective circulation when $Ra_{eq}$ is 6000. The thermal structure of the flow is very different from that calculated when the Rayleigh is 45 (Fig. 15). In particular, the thermal field is quasi symmetric about a line joining the upper right corner to the lower left corner of the box. It implies that the region along the axis of the crater is particularly cold: its temperature is close to the minimum surface air temperature (273.5 K). The surface temperature in the rim crest region remains roughly constant and close to that of the bottom of the crater ($T_{bottom} = 288.5$ K).

We observe a periodic cold plume developing just below the surface of the crater center. The detachment of each plume occurs about every 30 h. The Darcy velocity of the air below the center reaches about 20 cm $s^{-1}$. The isotherms are advected at a velocity $(\gamma u, \gamma w)$ of about 20 cm $s^{-1}$. When the detached cold plume reaches approximatively the mid-depth of the box, a new one forms at the crater center. At that time, the convective cell is entirely confined inside the cone. The variations of temperature during a daily cycle are small enough that the 20 cm $h^{-1}$-thermal waves equilibrates with basaltic aggregates of 10 cm (the larger grains at Formica Leo). The calculated surface temperatures at distinct moments, presented in Fig. 17, show a rim to crater center temperature drop up to 13 K. The shape of this profile differs from that of the $Ra_{eq} = 45$ model (Fig. 16).

*5.5.2. Fitting calculated surface temperatures at midnight with observed ones*

The $Ra_{eq} = 45$ model explains the observed rim crest to crater center temperature drop but not its shape. The temperature profile for the $Ra_{eq} = 6000$ model matches the observed shape, while its amplitude is generally twice as large, except when the cold plume has just detached from the top convective layer (Fig. 18). The shape of the temperature profile is matched for high permeabilities, i.e. in the range 1000–6000. The convection develops progressively and becomes more and more vigourous between $Ra_{eq} = 45$ and $Ra_{eq} = 6000$. This is the reason why we only shown two models at the extremities of permitted $Ra_{eq}$ range. The bottom temperature of the crater $T_{bottom}$ with a soil conductivity of $k = 0.4$ W $m^{-1}$ $K^{-1}$ yields a surface conductive heat flux $k\Delta T/H$ of 200 mW $m^{-2}$. In the model, air convection in the crater enhances the heat transfer by an order of magnitude. Thus, when $Ra_{eq} = 6000$, the heat flux at the surface is $x$ 2000 mW $m^2$, i.e. twice the heat flux estimated in the surrounding regions (Section 3). This disequilibrium cannot be maintained for a long period of time. It is likely that the temperature at the bottom of the crater $T_{bottom}$ will decrease gradually. If we still assume an effective Rayleigh number of $Ra_{eq} = 6000$, but an equilibrium heat flux of 1000 mW $m^2$, we can drop by a factor of 2 to $\Delta T$ to 3.5 K and increase the permeability by the same factor. This change does not modify $\gamma Ra$, implying that the surface temperature profiles when $\Delta T = 3.5$ K and $K = 2 \times 10^{-5}$ $m^2$ would only differ from those of Fig. 18 by the scale of temperature which would be divided by 2. Such a change would yield an excellent fit between computed and observed profiles.

## 6. Conclusion

Thermal Infrared images obtained during a diurnal cycle of the 250 years-old small inactive scoria cone of Formica Leo (Piton de la Fournaise volcano, Reunion Island) have been studied. Outside the cone, the surface temperature is explained by insolation and soil thermal conductivities. Inside Formica Leo, just before the dawn, the rim crests are warm compared to the crater centers. We demonstrate that air convection within the craters can explain the observed temperature pattern, provided the soil permeability is high ($\sim 10^{-5}$ $m^2$, a value consistent with the pluricentimetric scorias composing the cone). Then, the downward interstitial air velocity at the center of the crater is of the order of 50 cm $s^{-1}$, a value commensurable with the one deduced by the anemometer measurements. The equations describing air convection in the soil are the same than those of water convection, if we multiply the Darcy velocity of air and the Rayleigh number by $\gamma$, the ratio of the heat capacity of air to that of the soil (Eq. (10)). With such a permeability, it is important to mention that the Rayleigh number of porous convection for water saturated soil would be extremely elevated ($3 \times 10^5$). In this case, turbulent flows with very thin boundary layers and small plumes would lead to surface temperatures pattern clearly undetectable at 100 m distance with the IR camera. In the case of air convection, low Rayleigh numbers lead to laminar flows in larger plumes and surface temperature pattern detectable with the IR camera.

The convection of air in Formica Leo is a transient process, as described in our model. Indeed, porous flow within an open-top inclined layer leads to unsteady flow due to the development of hot transient plumes at the bottom boundary layer (Rabinowicz et al., 1999). Here, because of the diurnal temperature fluctuations, the soil surface is alternatively cooler and hotter than the air above the cone. It results that there are moments during which the flow is strictly confined within the cone and phases during which it is opened upward. As a result, a top convective boundary layer develops.

Fluctuations in this boundary leads to the periodic development of cold plumes which sink within each crater center. The strength of the flow dramatically increases during the phase of detachment of this plume. Note that the cyclicity of the plume is completely different from that of the diurnal cycle. The occurrence of these alternating regimes is strongly dependent on permeability. The flow is not confined for periods up to several days at the condition that the permeability is high and actually close to an upper bound of reasonable estimates ($10^{-5}$ $m^2$). During all these sequences, the lower boundary layer remains steady implying that no transient hot plumes take birth at the vicinity of the massive basalts lower boundary. Our models are bidimensional. It is clear that because of the conic shape of the structure, the axial deeping current will also mark the 3D pattern of convection in Formica Leo. But, a splitting of the upwelling flow along the rim of the cone is likely possible (Caltagirone and Boriès, 1985; Ormond et al., 1995). It is not clearly seen on the IR images (Fig. 5), indicating that the dominant mode of air convection is circular along the rims. Therefore, future studies of the thermal field of Formica Leo based on temperature probes measurement and electromagnetic data will provide complementary information of the tridimensional structure of the flow along the rim.

Our study constitutes the first demonstration that air convection can transport significant amount of heat within PdF volcano. Indeed, the volcanic edifice is composed by many highly permeable materials (e.g., fractures, scorias layers, buried scoria cones, lava tubes, etc...). IR images acquired at Bory Dolomieu crater (in particular, at fractured zones) in 2007 and 2008 also suggest that these regions are affected by air convection. Bory Dolomieu crater, where most eruptions initiated, presents a conic permeable structure with 30° slopes which rims are clearly warmer at night than the center of the crater. We believe that the understanding of the relationships between the ascent of the magma and the convection of air would make in the future a significant contribution for the prediction of volcanic hazards.


## Acknowledgements

This study beneficited from a grant INSU-CNRS 'Programme Catastrophes naturelles et tsunamis 2006' VOLCARISK. The Ph.D. thesis of Raphael Antoine was supported by Region Reunion. We thank Dr. William Wilcock and Dr. Lionel Wilson for constructive reviews that helped improve the clarity of the paper.


## Appendix A. Modelling diurnal temperature variations assuming a flat surface: the conductive–radiative model

The transient temperature in the soil, $T(z, t)$ is solution of the equation:

$$\frac{\partial T(z,t)}{\partial t} = \kappa \frac{\partial^2 T(z,t)}{\partial z^2} \tag{.1}$$

where $z$ is the depth, $t$ is the time and $\kappa$ is the thermal diffusivity of the soil, which is related to the thermal conductivity $k$, the heat capacity $C_p$ and the mass density $\rho$ of the soil through:

$$\kappa = \frac{k}{nh_s} \tag{.2}$$

A zero heat flux condition is set at the lower boundary of the model. For a flat surface, the surface temperature during a diurnal cycle depends on the solar heat flux ($I_s$), the soil radiative emission ($I_e$), and the atmospheric radiative flux ($I_l$). Thus, the boundary condition at the surface is given from the balance of solar, atmospheric and emitted radiations (Watson, 1973):

$$k\frac{\partial T(z=0,t)}{\partial t} = I_s - I_e + I_l \tag{.3}$$

The solar flux $I_s$ absorbed by the surface verifies:

$$I_s = (1 - A)S_0 C\cos(Z) \tag{.4}$$

where $A$ is the surface albedo and $S_0$ is the solar constant. $C$ is fraction of the incident power arriving at the soil including the direct sun light and the diffuse radiations for a cloudy sky. $Z$ is the zenith angle of the sun which can be estimated from the latitude $\phi$ of the observation point (Watson, 1973):

$$\cos(Z) = \cos\phi\cos\delta\cos(\theta) + \sin\phi\sin\delta \tag{.5}$$

where $\delta$ is the solar declination as a function of the number of day in Jovian year $J$ (Deffie and Beckman, 1980) and is expressed here in radian:

$$\delta = 0.409\sin\left(\frac{2\pi}{365}J - 1.39\right) \tag{.6}$$

The longitude angle $\theta$ expressed also in radian corresponds to the time $t$ in hours past noon:

$$\theta = 2\pi^* \frac{t}{24} \tag{.7}$$

Then, the thermal emitted flux from the surface $I_e$ is given by:

$$I_e = \epsilon\sigma T^4 \tag{.8}$$

where $\epsilon$ is the soil emissivity averaged in the thermal infrared wavelengths and $\sigma = 5.67\times10^{-8}$ $JK^{-4}m^{-2}s^{-1}$ is the Stefan–Boltzman constant. The thermal radiations from the atmosphere $I_l$ are approximated following the empirical relation (Brunt, 1932):

$$I_l = \sigma T_a^4(0.55 + 0.65^*\sqrt{e_a}) \tag{.9}$$

where $T_a$ is the air temperature in Celsius degrees and $e_a$ is the saturation pressure of water in the air expressed in bar. $T_a(t)$ is approximated by Jansson (1998):

$$T_a(t) = T_0 + \frac{1}{2}T_{amp}\cos\frac{2\pi\left(t - t_{ph}\right)}{P_{dc}} \tag{.10}$$

where $T_0$ is the mean air temperature during the diurnal cycle, and $T_{amp}$ is the contrast of temperature between day and night as measured during the experiment. $P_{dc}$ represents the duration of the diurnal cycle and $t_{ph}$ is the time shift between the maximum of the solar incident radiations and the maximum air temperature. This model results in a minimum air temperature at the sunrise and a maximum air temperature at $t_{ph}$ after the zenith. Finally, $e_a$ verifies the empirical law (Deffie and Beckman, 1980):

$$e_a = 0.6108\,exp\left(\frac{17.27^*T_a(t)}{T_a(t) + 237.3}\right) \tag{.11}$$

## References


Baytas, A.C., Pop, I., 1999. Free convection in oblique enclosure filled with a porous medium. Int. J. Heat Mass Transfer 42, 1047–1057.

Bonneville, A., Vasseur, G., Kerr, Y., 1985. Satellite thermal infrared observations of Mt. Etna after the 17th March 1981 eruption. J. Volcanol. Geotherm. Res. 24 (3–4), 293–313.

Boriès, S.A., Combarnous, M.A., 1972. Natural convection in a sloping porous layer. J. Fluid Mech. 57, 63–79.

Brivio, P.A., Lo Guidice, E., Zilioli, E., 1989. Thermal infrared Surveys at vulcano Island: An experimental Approach to the thermal monitoring of volcanoes, in *Volcanic Hazard*, edited by Springer–Verlag, pp. 357–371, IAVCEI Proceedings in volcanology, J.H. Latter ed., Berlin, 1989.

Brunt, D., 1932. Notes on radiation in the atmosphere. Quart. J. Roy. Meteorol. Soc. 58, 389–420.
Caltagirone, J.P., Boriès, S.A., 1985. Solution and stability criteria of natural convective flow in an inclined layer. J. Fluid Mech. 155, 267–287.
Carman, P.C., 1961. L'écoulement des gaz à travers les milieux poreux, Bibliothèque des Sciences et des techniques nucléaires. Press Universitaires de France, Paris. 198 pp.
Cherkaoui, A.S.M., Wilcock, W.S.D., 1999. Characteristics of high Rayleigh number two-dimensional convection in an open-top porous layer heated from below. J. Fluid Mech. 394, 241–260.
Chevalier, S., Bernard, D., Joly, N., 1998. Natural convection in a porous layer bounded by impervious domains: from numerical approaches to experimental realization. Int. J. Heat Mass Transfer 42, 581–597.
Chongbin, Zhao, Hobbs, B.E., Ord, A., Shenglin, Peng, Mühlhaus, H.B., Liangming, Liu, 2004. Theoretical investigation of convective instability in inclined and fluid-saturated three-dimensional fault zones. Tectonophysics 387, 47–64.
Christensen, P.R., Bandfield, J.L., Hamilton, V.E., Howard, D.A., Lane, M.D., Piatek, J.L., Ruff, S.W., Stefanov, W.L., 2000. A thermal emission spectral library of rock-forming minerals. J. Geophys. Res. 105 (E4), 9735–9739.
Coret, L., Briottet, X., Kerr, Y.H., Chehbouni, A., 2004. Simulation study of view angle effects on thermal infrared measurements over heterogeneous surface. IEEE Trans. Geosci. Remote Sens. 42 (n°3), 664–672.
Deffie, J.A., Beckman, W.A., 1980. Solar Engineering of Thermal Processes. John Wiley and sons, New York, pp. 1–109.
Douglas, J., Rachford, G., 1956. On the numerical solution of heat solution problems in two and three variables. Trans. Am. Math. Soc. 82, 421–439.
Fontaine, F., Rabinowicz, M., Boulègue, J., Jouniaux, L., 2002. Constraints on hydrothermal processes on basaltic edifices: inferences on the conditions leading to hydrovolcanic eruptions at Piton de la Fournaise, Reunion Island, Indian Ocean. Earth Planet. Sci. Lett. 200 (1–2), 1–14.
Jansson, P.-E., 1998. Simulation Model for soil water and heat conduction — Description of soil model, PhD thesis, Swedish University of Agricultural Sciences, Uppsala.
Kurita, K., et al., 2007. Thermal imaging of volcanic areas and implications for the interpretation of surface temperatures on mars. Seventh International Conference on Mars. Pasadena, California, USA. 3113 pp.
Lardy, M., Tabbagh, A., 1999. Measuring and interpreting heat fluxes from shallow volcanic bodies using vertical temperature profiles: a preliminary test. Bull. Volcanol. 60 (6), 441–447.
Myers, V.J., Heilman, M.D., 1969. Thermal infrared for soil temperature studies. Photogrammetr. Ing. J. 35, 1024–1032.
Ormond, A., Boulgue, J., Genthon, P., 1995. A thermoconvective interpretation of heat flow data in the area of Ocean Drilling Program Leg 116 in a distal part of the Bengal Fan. J. Geophys. Res. 100 (B5), 8083–8095.
Rabinowicz, M., Rouzo, S., Sempere, J.-C., Rosemberg, C., 1993. Three-dimensional mantle flow beneath mid-ocean ridges. J. Geophys. Res. 98 (B5), 7851–7869.
Rabinowicz, M., Boulègue, J., Genthon, P., 1998. Two- and three-dimentionnal modeling of hydrothermal convection in the sedimented Middle Valley segment, Juan de Fuca ridge. J. Geophys. Res. 103 (B10), 24045–24065.
Rabinowicz, M., Sempéré, J.C., Genthon, P., 1999. Thermal convection in a vertical slot: implications for hydrothermal circulation along mid-ocean ridges. J. Geophys. Res. 104 (B12), 275–292.
Rose, A.W., Guo, W., 1995. Thermal convection of soil air on hillsides. Environ. Geol. 25 (4), 258–262. doi:10.1007/BF00766755.
Rosenberg, N.J., Spera, F.J., Haymon, R.M., 1993. The relationship between flow and permeability field in seafloor hydrothermal systems. Earth Planet. Res. Lett. 116, 135–153.
Rowan, L.C., Offield, T.W., Watson, K., Cannon, J.P., Watson, R.D., 1970. Thermal infrared investigations, Arbukle mountains, Oklahoma. Geol. Soc. Amer. Bull. 81, 3549–3562.
Sabins, F.F., 1969. Thermal infrared imagery and its application to structural mapping in southern California. Geol. Soc. Amer. Bull. 80, 397–404.
Sturm, M., 1991. The role of thermal convection in heat and mass transport in the subarctic snow cover. USACRREL Report 91–19, 84 p.
Sturm, M., Johnson, J.B., 1991. Natural convection in the subarctic snow cover. J. Geophys. Res. 96 (11), 657–671.
Turcotte, D.L., Schubert, G., 2002. Geodynamics. Cambridge University Press. 456 pp.
Watson, K., 1973. Periodic heating of a layer over a semi-infinite solid. J. Geophys. Res. 78 (26), 5904–5910.
Watson, K., 1975. Geologic applications of thermal infrared Images. Proc. IEEE 63, 128–137.
Whiteman, C.D., Allwine, J., Fritschen, L.J., Orgill, M.M., Simpson, J.R., 1989. Deep valley radiation and surface energy budget microclimates, Part I: Radiation. J. Appl. Meteorol. 28, 414–426.
Whiteman, C.D., Zhong, S., Bian, X., Fast, J.C., Doran, J.C., 2000. Boundary layer evolution and regional-scale diurnal circulations over the Mexico Basin and Mexican plateau. J. Geophys. Res. 105 (D8), 10081–10102.
Wood, J.R., Hewett, T.A., 1982. Fluid convection and mass transfer in porous sandstones — a theoretical model. Geochim. Cosmochim. Acta 46, 1707–1713.
Woodside, W., Messmer, J.H., 1961. Thermal conductivity of porous media: I Unconsolidated sand,. J. Appl. Phys. 32, 1688–1691.
Yu, W., Lai, Y., Zhang, X., Niu, F., 2005. Experimental study on the ventiduct embankment in permafrost regions of the Qinghai–Tibet railroad. J. Cold Reg. Eng. 19 (2), 52–60. doi:10.1061/(ASCE)0887-381X(2005)19:2(52).
Zhang, M., Zhang, J., Yuanming, L., 2005. Numerical analysis for critical height of railway embankment in permafrost regions of Qinghai–Tibetan plateau. Cold Reg. Sci. Technol. 41 (2), 111–120.